

A Balance between Inter- and Intra-Microgel Mechanics Governs Stem Cell Viability in Injectable Dynamic Granular Hydrogels

Cameron D. Morley, Erika A. Ding, Emily M. Carvalho, and Sanjay Kumar*

Injectable hydrogels are increasingly explored for the delivery of cells to tissue. These materials exhibit both liquid-like properties, protecting cells from mechanical stress during injection, and solid-like properties, providing a stable 3D engraftment niche. Many strategies for modulating injectable hydrogels tune liquid- and solid-like material properties simultaneously, such that formulation changes designed to improve injectability can reduce stability at the delivery site. The ability to independently tune liquid- and solid-like properties would greatly facilitate formulation development. Here, such a strategy is presented in which cells are ensconced in the pores between microscopic granular hyaluronic acid (HA) hydrogels (microgels), where elasticity is tuned with static covalent intra-microgel crosslinks and flowability with mechanosensitive adamantane-cyclodextrin (AC) inter-microgel crosslinks. Using the same AC-free microgels as a 3D printing support bath, the location of each cell is preserved as it exits the needle, allowing identification of the mechanism driving mechanical trauma-induced cell death. The microgel AC concentration is varied to find the threshold from microgel yielding- to AC interaction-dominated injectability, and this threshold is exploited to fabricate a microgel with better injection-protecting performance. This delivery strategy, and the balance between intra- and inter-microgel properties it reveals, may facilitate the development of new cell injection formulations.

the anatomical target is diffuse, such as in the case of bone marrow transplantation, cells may be delivered intravenously, leveraging diffusion and convection through the vasculature for distribution throughout the body. However, highly localized delivery of cells to solid tissues has proven much more challenging because the formulation must be sufficiently liquid-like to permit injection but sufficiently solid-like to remain at the target site. Encapsulation of cells in 3D hydrogels prior to injection into tissue is emerging as an attractive strategy to address the latter challenge.^[1–5] Once delivered, hydrogels can provide a mechanically stable engraftment niche for engineered cells and thus improve cell survival and function.^[3,6] However, the covalent crosslinking strategies often used to form these hydrogels can compromise injectability and potentially subject cells to mechanical trauma as the hydrogel can be damaged during injection.^[7,8] Viability and engraftment in vivo can often fall below 5%,^[3,6] which has been attributed to the possibility that rheological characterization alone may inadequately capture the injectable's injection-protecting properties

during flow through thin needles and under the near-instantaneous deformation associated with hand injection.^[9] Thus, there is a strong and open opportunity to improve the performance of shear-thinning injectables by better-defining relationships between injectable composition, flow properties, and cell viability.

Progress has been made by developing hydrogels with temporally tunable crosslinking kinetics, such as those employing click-chemistries^[10–12] or self-healing materials that respond to external stimuli (e.g., pH or temperature),^[13,14] and shear-thinning properties to facilitate flow during injection and control over solidification upon delivery.^[15–18] An emerging mechanosensitive crosslinking approach creates dynamic noncovalent crosslinks using guest-host chemistries,^[19] such as adamantane and cyclodextrin (AC),^[5,20] allowing for transient rupture and bond reformation in response to shear stress. Hydrophobic and highly specific AC interactions^[14,21] facilitate the rapid dissociation and re-association of bonds required to satisfy the two dominant goals of injectable cell carriers. While dynamic crosslinking strategies

1. Introduction

Administration of cell-based therapeutics has shown increasing promise for disease treatment and regenerative medicine. When

C. D. Morley, S. Kumar
Department of Bioengineering
University of California
Berkeley, CA 94720, USA
E-mail: skumar@berkeley.edu

E. A. Ding, E. M. Carvalho, S. Kumar
Department of Chemical and Biomolecular Engineering
University of California
Berkeley, CA 94720, USA

S. Kumar
Department of Bioengineering and Therapeutic Sciences
University of California
San Francisco, CA 94158, USA

 The ORCID identification number(s) for the author(s) of this article can be found under <https://doi.org/10.1002/adma.202304212>

DOI: 10.1002/adma.202304212

greatly improve the protection of cellular cargo in cell therapies, they fail to fully address the trade-off between injectability and stability; enhancing performance in one property generally compromises the other. Independent tuning of material injection protection and engraftment facilitation is needed to improve the efficiency of cell therapies.

Packed microscale hydrogel particles (microgels), which are widely used in 3D cell culture and biofabrication,^[22–25] have recently been explored as a strategy for balancing injectability and injection-protection.^[26–30] In the jammed state, these materials reconfigure and flow like liquids at high shear rates but also demonstrate solid-like yield stress properties at low shear rates.^[22] The micro-porous architecture of microgels facilitates cell encapsulation between particles, which physically shields cells from intra-needle velocity gradients and high shear stresses at the no-slip boundaries. Previous studies have shown that particle shape and size influence injectability and engraftment,^[27,28] and dynamic inter-particle AC crosslinking improves injection protection and viability for cells encapsulated between spherical but not irregularly shaped particles.^[28] An appealing explanation for the latter result is that the increased contact area and inter-particle interaction associated with fragmented particles may alter rheological properties and consequently injectability and cell viability.^[28] A deeper understanding of how the balance between intra- and inter-particle interactions affects cell injection and cell viability would facilitate customized injection protection for future cell therapies.

In this study, we introduce an injectable formulation strategy in which spherical hyaluronic acid (HA) microgels are dynamically crosslinked with AC and decorated with RGD-based peptides to enable 3D integrin engagement. Just as the force-sensitivity of AC crosslinks has been exploited to fabricate stress-relaxing bulk hydrogels, we find that reversible AC crosslinks between microgel particles support the shear-thinning behavior needed for injectability while stabilizing the microgel pack post-injection with minimal residual stress. We demonstrate the ability to independently tune the elastic and flow properties of the microgel pack by varying HA and AC concentration, respectively. We also explore the effects of the balance between static intra- and dynamic inter-microgel properties on injected cell viability.

2. Results

2.1. Microgels as an Injectable and as a Platform for Injectable Testing

2.1.1. HA Microgel-Based Injection-Protecting Formulation

Guest-host microgel formulations have emerged as a promising strategy for cell delivery, primarily due to their injection-protecting nature. However, the governing principles that relate microscale mechanics within the microgel formulation to injection protection and injectability remain incompletely understood. We hypothesized that the flow properties of guest-host microgels are dictated by a balance between the intrinsic material properties of the microgels themselves and the strength of the AC bonds between microgels. We further reasoned that we could tune cell survival by first modifying inter-microgel interactions alone.

To systematically explore these governing principles, we fabricated spherical HA microgel assemblies stabilized by two types of crosslinks: static covalent linkages to set intrinsic microgel mechanical properties, and dynamic AC-based inter-microgel crosslinks that can break and reform. To introduce chemical handles for both crosslinking and peptide conjugation, we methacrylate-functionalized HA (MeHA) (Experimental Section, Figure S1, Supporting Information).^[31,32] We then fabricated monodisperse ($n = 100$ measurements, PDI = 0.01), 10.0 μm diameter (Figure S2a–c, Supporting Information) spherical microgels by reacting 2% (w/w) MeHA with a 1,4-dithiothreitol (DTT) crosslinker in the aqueous phase of an inverse emulsion (Experimental Section, Figure 1a). We tuned the microgel diameters to be cell-sized, minimizing intra-needle velocity gradients by ensuring that both cells and microgels are roughly 10 \times smaller than the 200 μm (27–30G) cannula diameter commonly used in the delivery of cell therapies^[9] (Figure 1b). We functionalized the microgels with RGD and AC, centrifuged them to mimic the mechanical properties of their bulk hydrogel counterparts (Experimental Section, Figure S3b, Supporting Information), and mixed them with cells before testing their efficacy at reducing intra-needle shear stress and facilitating 3D engraftment (Figure 1c).

2.1.2. Material Platform Validation – Neural Stem Cell (NSC)-Microgel Attachment

Prior to mechanically characterizing the governing relationships between microgel mechanics, injectability, and cell viability, we sought to establish the baseline ability of our microgel formulation to support cell adhesion and function, particularly the ability to form multicellular assemblies, protrusions, and cell-cell connections. For our studies, we chose to work with murine neural stem cells (NSCs, Experimental Section), which can give rise to neurons in the brain and show great promise as injectable cell sources in neuroregenerative applications^[3,33,34] but suffer from low rates of engraftment. To facilitate NSC attachment, we functionalized the microgels with an RGD-based adhesive peptide (Experimental Section) and gently pipette-mixed them with NSCs to create homogenous 3D cellular dispersals.

NSC viability was sensitive to 2D seeding density, leading us to consider the effect of seeding density on viability and attachment in 3D as well. We found seeding densities, ϕ_0 , below 10% (v/v) to have low viability in bare microgels beyond 3 days in culture (Figure S4, Supporting Information), so we examined attachment of NSCs seeded at $\phi_0 = 10\%$ in microgels functionalized with 0–0.2 mg mL^{-1} RGD peptide. After 24 h in 3D culture, NSCs in microgels of all RGD concentrations microgels self-assembled into spheroids and began extending protrusions into the microgel pack (Figure 2a and Figure S6, Supporting Information). With additional time in culture, protrusions began to connect spheroids, where we noticed the z-position of spheroid-connecting protrusions depended on RGD concentration. NSCs cultured in bare and 0.002 mg mL^{-1} RGD microgels generated protrusions only at the interface of the glass bottom of the well ($z = 0 \mu\text{m}$) (bottom panel, Figure 2a,b, Experimental Section), indicating that NSCs do not efficiently form 3D connections in these conditions. Instead, only small, discrete spheroids are observed at large z-depths (white circles, Figure 2a, bottom). In contrast,

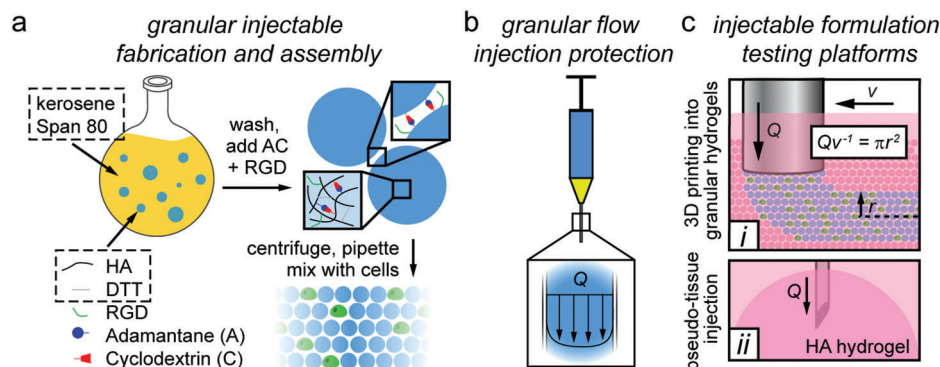


Figure 1. Microgel-based injectable assembly and testing platform. a) Inverse emulsion polymerization process of MeHA and DTT. Residual methacrylate groups are used for functionalization with AC and RGD-based cell adhesion peptides. Cells are encapsulated between these microgel particles to b) facilitate injection protection and provide a stable 3D engraftment niche post-injection. c) 3D printing platform used to facilitate the study of injection protection and retention.

network-forming protrusions can be observed hundreds of microns above the glass bottom in 0.02 and 0.2 mg mL⁻¹ RGD microgel packs (Figure 2a,b). Increasing NSC density to 20% (v/v) led NSCs to assemble more quickly (Figure 2b) but with shorter connecting protrusions. The slower NSC assembly with greater cell-to-cell distance (Figure 2b) is consistent with previous studies demonstrating a percolation threshold for cellular dispersals in granular media.^[25] Based on these results, we used 10% (v/v) cell densities in subsequent injection experiments.

2.1.3. Material Platform Validation – NSC Injection into Hydrogels

Based on the expectation that cells could attach to the injected matrix in 3D, we next asked whether the microgel injectable improves NSC engraftment potential by retaining more injected cells. We injected NSCs mixed with either liquid medium or bare HA microgels into bulk HA hydrogels using the injector of our 3D bioprinter (Figure 3a, Experimental Section). While this injection strategy is a heavily abstracted model of in vivo injection, the use of a hydrogel target rather than tissue enabled us to visu-

alize the injected volume to measure the retained injectable volume, V_r , with confocal microscopy. Moreover, the use of precise linear motion stages allows us to delicately enter tissue-like hydrogels and evaluate the volume of cargo retained when injected into viscoelastic solids. After 12 h of 3D culture post-injection, we observed viable cells in both the microgel and liquid media injectables, albeit with distinctly unique injected volumetric morphologies (Figure 3b). In contrast, the yield stress capability of the microgel injectables reinforced the cracks generated by injection and deformed the hydrogel to create a larger oval-shaped cavity (Figure 3b). We measured a 7.5-fold increase in retention volume for the microgel injectable relative to the liquid medium control ($p < 0.01$) (Figure 3c, Experimental Section and Supporting Information).

2.1.4. 3D Printing into Microgels: Determining Sources of Mechanical Trauma in Granular Injectables

Having established that our microgel formulation supports NSC adhesion, viability, and retention upon injection into hydrogels,

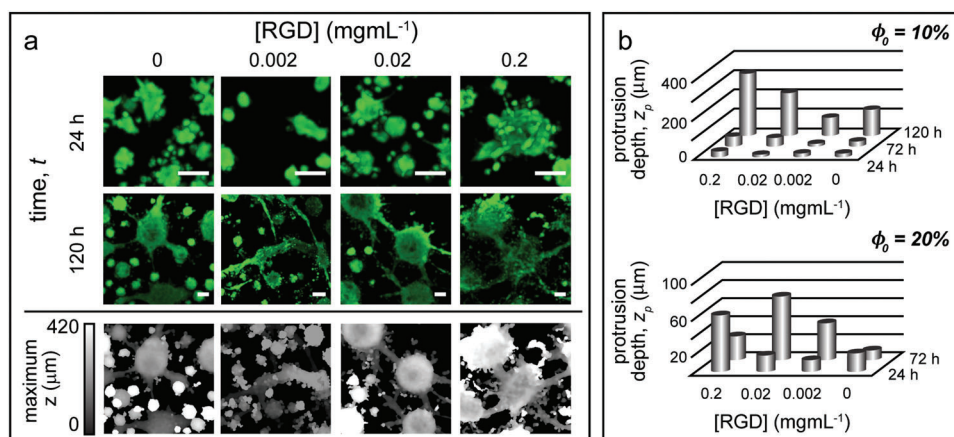


Figure 2. Quantifying 3D NSC attachment. a) Representative images of the dominant morphological phenotype for each RGD concentration and $\phi_0 = 10\%$ – (top) maximum intensity projection of raw fluorescent data – (bottom) grayscale heightmap used to calculate protrusion depth. Scale bars = 50 μm . b) Quantification of maximum protrusion depth as a function of seeding density, ϕ_0 , and time, t . Bars represent the mean maximum protrusion depth ($n = 3\text{--}5$ measurements).

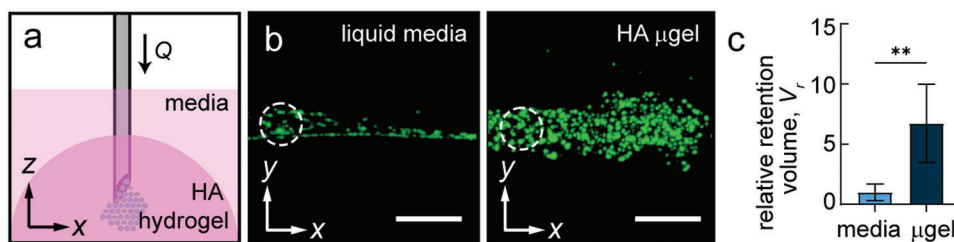


Figure 3. Retaining injected cellular cargo. a) Injection into hydrogels to measure the volume retention capacity of granular materials. b) Representative images of NSC-laden liquid (left) and NSC-laden microgel (right) injectable. Images shown are maximum intensity projections of confocal z-stacks. The white dotted circle represents the 30G needle diameter. Scale bar = 250 μm . c) Quantification of relative retention volume, V_r ($n = 3$ samples, data reported as mean \pm SD, $p < 0.01$).

we next investigated the ability of our microgel-based formulations to support injection protection and cell viability during injection using our 3D bioprinter. We compared the performance of our microgel formulations against control conditions in which NSCs were suspended in non-crosslinked hydrogel precursor solutions. Testing injectable efficiency using this embedded 3D printing approach holds many key strategic advantages. Precise control of flow rate with our 3D printer enables the prediction of intra-injectable stresses when coupled with rheological characterization. Most importantly, embedded printing in microgels preserves the spatial distribution of cells as they exit the needle, allowing us to identify the localization of cell damage. When injecting Newtonian or shear-thinning liquids, for example, we would expect mechanical stress-induced cell death to be highest at the needle wall and gradually decrease toward the center of the needle. If this cargo was being injected into liquid media, the shear history of each cell would be lost, eliminating the ability to directly observe cell death at the no-slip, high-shear stress boundary. Access to injection history could be informative in developing injectable formulations, especially for non-Newtonian or granular microgel injectables, where the flow profile is rate-dependent and underlying injection-protection limitations are still poorly understood.^[9,28]

To first demonstrate that embedded 3D printing preserves the injection history and quantify the shear stress required to damage NSCs, we printed mixtures of NSCs with the microgels' Newto-

nian liquid precursor, 3% (w/w) uncrosslinked MeHA, into bare (i.e., free of AC and RGD) HA microgels. We chose the MeHA concentration by identifying the viscosity and shear rate required to generate 5–100 Pa of shear stress at the needle wall, as previous reports document cell death and membrane rupture between 30–150 Pa^[35,36] (Figure 4a, Supporting Information). To increase shear stress, we varied the shear rate from 250–4125 s^{-1} , and modified the printing needle translational velocity proportionally to achieve 300 μm printed diameters, thereby minimizing potential negative effects of nutrient depletion at the center of printed NSC features in 3D culture. We confirmed the Newtonian fluid-like behavior of MeHA by showing $\sigma \dot{\gamma}$ across the range of tested shear rates with unidirectional rheology (Figure S3a, Supporting Information). We predict printed feature cross-sectional area, A , similar to our previous reports^[22] (Experimental Section, Figure S7, Supporting Information). In these MeHA prints, we observed increased cell death (red, Figure 4a, Experimental Section) with increasing shear rate and localization of dead cells at the outermost layer of the printed object.

We repeated the shear rate sweep with mixtures of bare microgels and NSCs into bare HA microgels and found increased cell viability relative to their liquid MeHA counterparts. However, cell viability at the highest shear rate still fell below 70%, which is required for FDA approval of injectable cell formulations.^[37] In contrast to the MeHA prints, we observed dead cells and increasing co-localization of the live and dead channels distributed

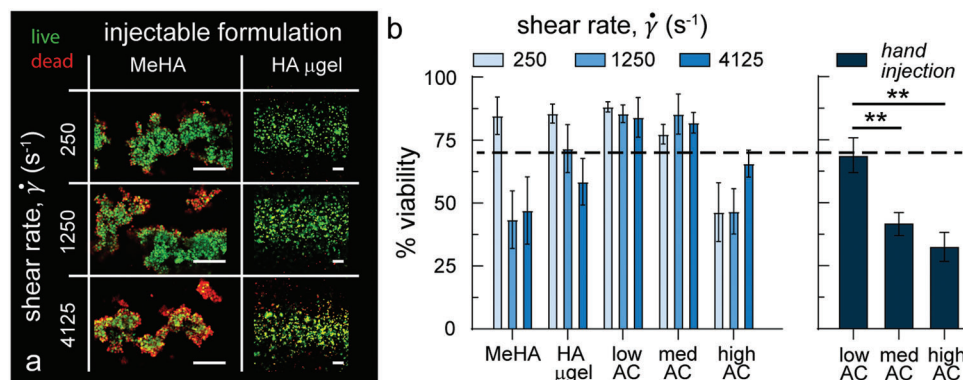


Figure 4. 3D printing injectable formulations into bare HA microgels. a) Live (green) and dead (red) cells after 24 h in culture post-injection into our 3D printing sacrificial microgel material. Scale bar = 100 μm . Quantification of viability for cells injected b) at controlled shear rates on the 3D printer and hand injected. The dashed line corresponds to the 70% viability target. Data reported as mean \pm SD ($n = 3$ samples). Annotations of statistical significance are omitted (left) for clarity.

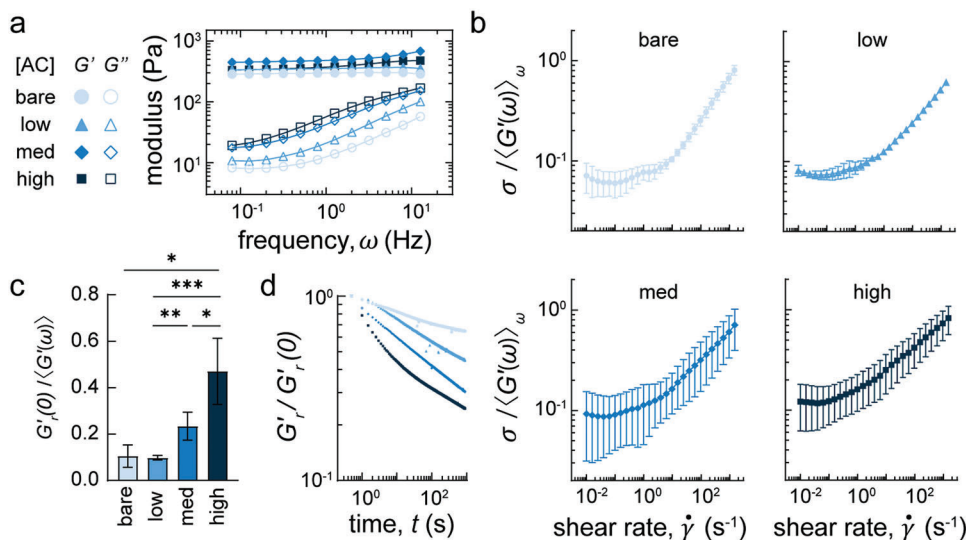


Figure 5. Rheological characterization of HA-AC microgels. a) Oscillatory rheology shows $G' > G''$ and frequency independence of G' for all AC concentrations. b) Unidirectional rheology is normalized by $\langle G'(\omega) \rangle_\omega$, from the oscillatory sweep to determine if they behave like HB yield stress fluids. Data reported as mean and error bars represent the minimum and maximum σ ($n = 3$ samples) for a given $\dot{\gamma}$. c) Peak relaxation modulus normalized by $\langle G'(\omega) \rangle_\omega$ to quantify the maximum stress upon instantaneous deformation. d) Full stress relaxation data normalized by $G'_r(0)$.

throughout the printed feature, suggesting shear stress is instead generated between microgels. We hypothesized that cellular damage could be driven by the increased frequency of microgel rearrangement and the speed at which microgels slide past one another at high shear rates.

To suppress microgel rearrangements and consequent intrajectable shear stress, we printed mixtures of NSCs and AC-functionalized HA microgels into bare HA microgels. We functionalized our HA microgels with AC concentrations of 0.01 (low), 0.05 (medium), and 0.11 (high) molecule-to-HA monomer repeat unit molar ratio and repeated the injection shear rate sweep (Experimental Section). We found that the low and medium AC densities support higher cell viability than MeHA, bare HA microgels, and high-AC microgels (Figure 4b). We then sought to further evaluate the performance of the AC microgel injectables under more realistic injection speeds, so we performed injections by hand (Methods) which we predict generates a shear rate 5-fold higher than the maximum shear rate of our 3D printer. Strikingly, we found that viability fell with increasing AC concentration ($p < 0.01$), and low AC concentration yielded 70% NSC viability (Figure 4b).

2.2. Determining the Mechanism for Decreased Cell Viability in High AC Concentration Microgels

The reduced cell viability in the high-AC concentration microgels suggests that increased microgel-microgel adhesion alters rheological properties in a way that reduces injection protection. Control experiments revealed that the cytotoxicity seen in these formulations could not solely be attributed to physical NSC-microgel contact or unreacted AC reagents (Experimental Section, Figures S4, S5a, and S8, Supporting Information). We also began to observe shear rate-dependent increases in cell death as early as 24 h post-injection (Figure S9, Supporting Information).

These studies support the notion that mechanical trauma dominantly contributes to cell death in our system. We also therefore chose to evaluate cell viability at 24 h post-injection in subsequent experiments.

Cell viability in our microgel injectable formulations appears to be independent of radial position, in contrast to injection with MeHA solution, implying that the microgels protect the NSCs from injection trauma at low shear rates. As the shear rate increases, cell death increases throughout the microgel but remains radially independent, implying that higher shear rates induce trauma driven by microgel rearrangement. The factors governing inter-microgel mechanics are the microgel yield stress, which is a function of intrinsic microgel material properties, and AC bond density. To quantify these factors, we probed microgel pack mechanics using rheology and HA hydrogel surface mechanics using atomic force microscopy (AFM).

2.2.1. Rheological Characterization of AC Microgel Packs

We first performed oscillatory rheology to measure the elastic storage modulus, G' , and the loss modulus, G'' , of each AC microgel condition (Figure 5a). For all AC concentrations, G' was frequency-independent and greater than G'' , indicating dominantly solid-like behavior at low strain. Further, we observed minimal changes in low-strain mechanical properties with increasing AC concentration, which is expected due to the molar ratio of DTT being much larger than that of the AC (Methods). Despite observing changes in G' that vary by less than a factor of two across all samples, we observed up to a 5-fold increase in G'' between the high AC concentration and bare microgels. This demonstrates that intra-microgel AC dominantly contributes to G'' in the limit of a much higher molar ratio of DTT, enabling us to tune elastic and flow properties independently. We then performed unidirectional rheology on the AC microgels and found

Table 1. Fitted values for rheological characterization (Figure 5b,d). Fitted parameters σ_y and $\dot{\gamma}_c$ (Experimental Section) are not calculable for med and high AC concentrations since they do not behave as HB yield stress fluids.

[AC]	σ_y/G'	$\dot{\gamma}_c [1 \text{ s}^{-1}]$	p	β
Bare	0.06	6.60	0.49	0.07
Low	0.07	10.53	0.43	0.12
Med	N/A	N/A	0.36	0.15
High	N/A	N/A	0.29	0.27

that bare and low AC microgels behave as Herschel–Bulkley (HB) yield stress fluids (Experimental Section, Figure S10a, Supporting Information). At low shear rates, $\dot{\gamma}$, HB materials display a plateau in shear stress, denoted as the material yield stress, σ_y , and at high shear rates they showcase constant, sub-Newtonian flow, where $\sigma \propto \dot{\gamma}^{-1}$. In contrast, medium and high AC concentration microgels do not have the characteristic plateau at low shear rates and can often display slip-like events, indicated by a gradual increase followed by a rapid decrease in σ (Figure S10b, Supporting Information). Shear stresses at a given single shear rate can also vary by more than half an order of magnitude (Figure 5b).

We repeated the oscillatory and unidirectional characterization of bare HA microgels from different MeHA stocks and microgel fabrications to ensure the reproducibility of the aberrant rheological properties (Figure S10a,c, Supporting Information). The measured G' and σ_y vary by less than a factor of 2, which is much less than the 5-fold change observed in σ_y for medium and high AC concentrations (Figure 5b). Thus, we attributed the small variation in bare HA microgel rheological properties to errors in sample preparation. Past studies have demonstrated that microgels display the linear scaling relationship, $G' \sim \sigma_y$.^[22,25,38] This relationship was leveraged to both account for sample preparation variability, as changes in G' would be reflected in σ_y , and to isolate the effect of AC bonds on flowability. For a given sample, we normalized σ from unidirectional rheology by its respective average G' from oscillatory rheology (Figure 5a) resulting in the expression, $\sigma / \langle G'(\omega) \rangle_\omega$, where ω is the frequency and plotted the average calculated values ($n = 3$ samples, Figure 5b) with error bars corresponding to the minimum and maximum shear stress at each shear rate.

These normalized data confirm the classification of the bare and low AC microgels as HB materials, where forced flow in these microgel packs generates measured σ_y on the order of 10% of G' and with minimal variation in σ for all shear rates. In fitting the bare and low AC microgels to the HB model, we found that the magnitude of the power-law increase in σ at high $\dot{\gamma}$ decreased with increasing AC concentration (Table 1). The trend of decreasing power-law with increasing AC concentration continues with the medium and high AC samples, suggesting that flow becomes less Newtonian and more shear thinning. However, the aberrant unidirectional rheology flow profiles for medium and high AC concentrations suggest that inter-microgel AC bonds play a larger role than the microgel yield stress during injection. We expect the maximum shear stress during microgel rearrangement to correspond to the bare microgel yield stress; however, AC bonds connecting microgels must break prior to microgel yielding for

this to be true. We therefore sought to quantify the maximum shear stress arising from microgel rearrangement, and experienced by cellular cargo, by applying an instantaneous step-shear to our HA-AC microgel formulations and measuring their relaxation moduli, G'_r (Figure 5c,d). We quantified the peak relaxation modulus, $G'_r(0)$, normalized by the samples' respective average G' from oscillatory rheology and observed an increasing maximum shear stress with increasing AC concentration (Figure 5c). The peak relaxation moduli of the bare and low AC concentration microgels were statistically indistinguishable, and their magnitude closely matched the bare microgel yield stress, corroborating our expected result. In contrast, instantaneously applied shear on high AC microgels can result in shear stresses up to five times the bare microgel yield stress. The values of peak relaxation moduli in medium and high AC microgels far exceed the bare microgel yield stress, suggesting yielding and microgel rearrangement are set by the strength of inter-microgel AC bonds instead of the microgel yield stress. The discrepancy between these peak moduli values and shear stress at low shear rates in unidirectional rheology supports the idea of highly unpredictable and rate-dependent flow properties for medium and high AC concentration microgels.

Examination of G'_r over time, t , reveals a power-law relationship (Figure 5d). Fitting these curves to the equation, $G'_r(t) = t^{-\beta}$, where β is the slope of the relaxation curve on a log-log scale, reveals increases in the magnitude of β with increasing AC concentration (Table 1). While the mechanism behind this scaling law requires further study, we attribute this feature to an increased rate of AC bond re-formation, likely due to increased AC bond density, after large shear events.

Taken collectively, we hypothesize that low AC concentrations enable the microgels to ease rearrangement during flow, protecting cellular cargo better than their bare microgel counterparts. This hypothesis is supported by the observation of a lower power scaling between σ and $\dot{\gamma}$ (Table 1). However, when AC bond density increases above a certain threshold, we reasoned that the stress required to break bonds at the microgel-microgel interface could be greater than the microgel yield stress, increasing the frequency and magnitude of microgel yielding and damaging cellular cargo.

2.2.2. Quantifying the Stress to Break AC Bonds

To quantify AC bond stress, we performed atomic force microscopy (AFM) on bulk HA-AC hydrogels with an adamantane-functionalized probe (Methods, Figure 6a). We observed a non-linear relationship between force and indentation depth, as measured by displacement into the sample (Experimental Section), d , on the approach curve (red, Figure 6b) between the adamantane-functionalized probe and all HA-AC hydrogels. The retraction curves (blue, Figure 6b) revealed large adhesion events; we observed a negative measured force when $d = 0 \mu\text{m}$ and negative measured values of d when the probe disengages with the hydrogel (black circle, Figure 6b). We analyzed the approach curves to calculate the elastic modulus, E (Figure 6b,c), and retraction curves to measure adhesivity, extracting work of adhesion, W_a , and maximum adhesion force, F_a (Experimental Section, Figure 6b). To ensure that the adhesion events were

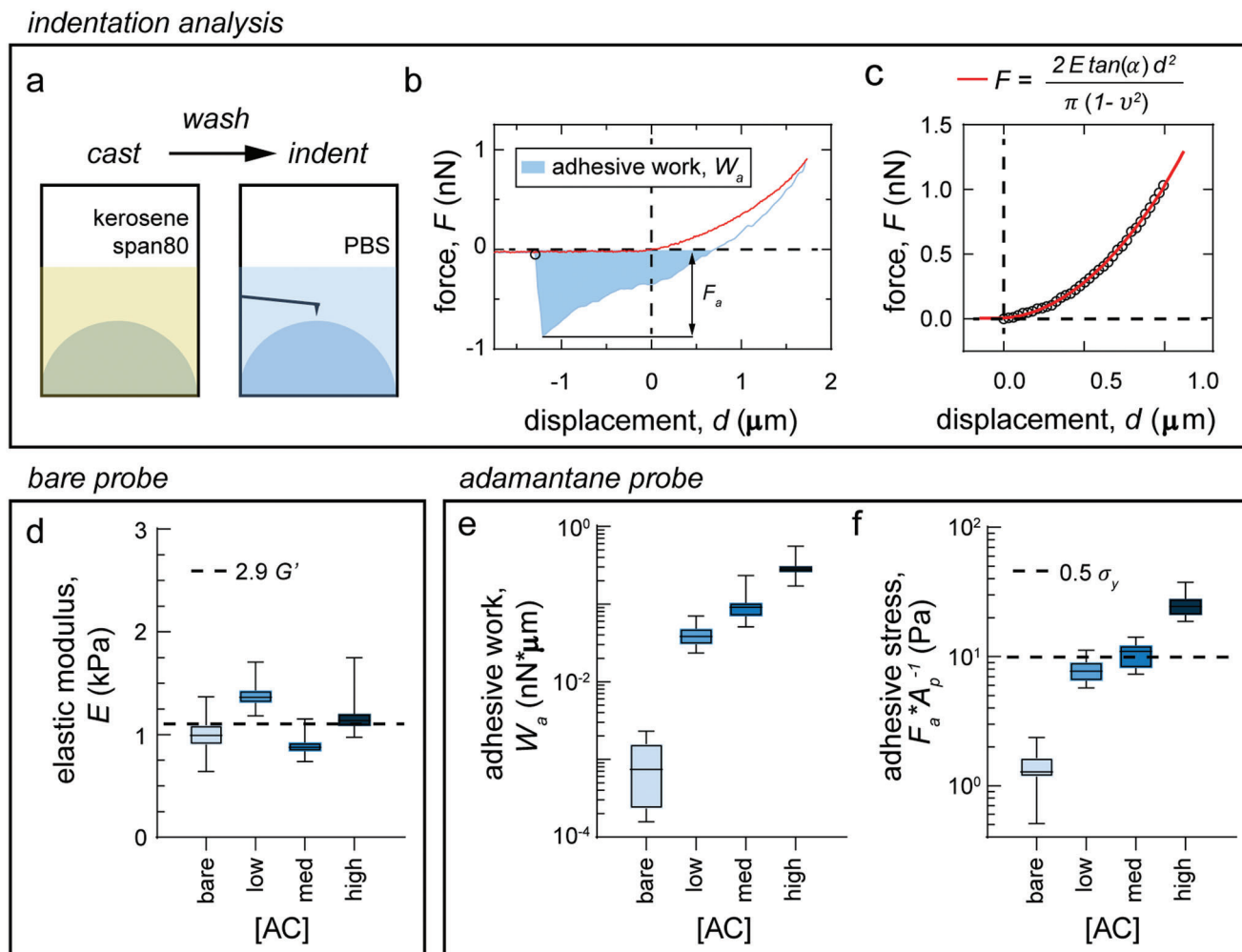


Figure 6. AFM on HA-AC hydrogels. a) Sample preparation for AFM measurements. b) Representative indentation and retraction curve including calculated metrics for quantifying adhesion. c) Representative indentation curve fitting using the approximation of Hertzian conical contact. d) Young's modulus values from curves acquired on samples with a bare probe. e) Adhesive work and f) adhesive stress calculation for AC samples indented with an adamantane functionalized probe. Box plots display the IQR and whiskers represent the 1st and 99th percentiles ($n = 100$ indentations with the bare probe and 36 indentations with the adamantane-functionalized probe). Annotations of statistical significance are omitted for clarity. Adhesive stress measurements between low and med AC concentrations significantly differ from one another by t -test ($p < 0.001$). All other adhesive work and stress measurement comparisons significantly differ from one another by t -test ($p < 0.0001$).

AC-specific, we performed indentations on HA-AC hydrogels with a bare probe. We observed that W_a and F_a fell in the measurement noise floor, closely mimicking the bare probe on bare hydrogel indentations (Figure S11a, Supporting Information). Fitting the data on the approach curves of these indentations, we calculate elastic moduli just above 1 kPa (Figure 6d). Using measured values of Poisson's ratio for these hydrogels (Figure S12, Supporting Information) and using the equation, $E = 2G'(1 + \nu)$, we find agreement between our rheological and AFM characterization (Figure 6d). This finding further corroborates the finding that AC contributes minimally to elasticity in this formulation.

In characterizing the retraction curves of HA-AC hydrogels indented with the adamantane-functionalized probe, we found adhesion increased with increasing AC concentration (Figure S11b,c, Supporting Information) and was minimal when indenting a bare hydrogel. This trend led us to conclude that adhesion

is dominated by specific AC interactions. We observed large adhesive forces over large retraction distances prior to AC bond disengagement, leading us to calculate W_a . We found that W_a increased with increasing AC concentration (Figure 6e). We calculated adhesive stress during AC bond-breaking by dividing F_a by the maximum measured probe contact area, A_p (Experimental Section). We also observed increasing adhesive stress with increasing AC concentration (Figure 6f) and sought to compare these values to the bare microgel yield stress. Since only half of the AC molecules are engaged during these experiments, we assume that we only measure half the stress required to break AC bonds between adjacent microgels. Thus, to compare the magnitude of the yield stress to the magnitude of the stress generated during AC bond-breaking between microgels, we compared the adhesive stress (Figure 6f) to half the bare microgel yield stress. Strikingly, we find the adhesive stress of the low and medium AC

Table 2. AC solution molarity corresponding to each molar ratio.

	AC:HA molar ratio		
	0.01	0.05	0.11
Final AC concentration [mM]	0.32	1.58	3.15

concentrations straddle the microgel yield stress line, supporting the hypothesis that breaking bonds in medium and high AC concentration microgels requires stresses larger than the bare microgel yield stress. This conservative approximation further supports the idea that a balance between two forces dictates injectability and cell survival in granular guest-host microgels.

2.2.3. Exploiting the AC Bond Strength and Microgel Yield Stress Threshold

The AFM results suggest that either decreasing the AC concentration or increasing the microgel yield stress could improve injected cell viability. The former would decrease the stress required to break inter-microgel connections, and the latter would increase the stress that the microgel pack could withstand upon AC bond-breaking events. To test this hypothesis and determine if the low AC concentration microgels were optimal for the 2% (w/w) microgel formulation, we fabricated microgels with 0.001 and 0.005 AC:HA ratios. We repeated hand injections with these microgels and compared their injection-protecting performance against bare microgels (Figure S13a, Supporting Information). However, we observed that lower AC concentrations resulted in marginally reduced viability that neared bare microgel injection levels (Figure S13c, Supporting Information) and AC-specific adhesivity similar to that of bare hydrogels (Figure S13b, Supporting Information).

We then tested the hypothesis that increased microgel yield stress could improve cell viability. To make microgels with a higher yield stress, we increased the MeHA concentration to 4% (w/w), fixing the DTT-to-HA monomer ratio at 0.7 and varying the AC molar concentration from 0.32–3.15 mM (Table 2). Oscillatory rheology shows that bare 4% (w/w) microgels have G'

of 3000 Pa and σ_y of 80 Pa, roughly 7.5- and 4-fold increases in these properties with respect to the 2% (w/w) microgels (Figure S14, Supporting Information). The yield stress of the 4% (w/w) microgels is twice the magnitude of the highest measured adhesive stress in the 2% (w/w) and 3.15 mM AC microgels, so we anticipate injection with this formulation would yield higher cell viability. We repeated the hand injection experiment (Figure 7a) and found viability substantially increased with the 4% (w/w) AC microgels relative to their 2% (w/w) counterparts for all AC concentrations. From this result, we conclude that granular guest-host injectable performance relies heavily on the interplay between microgel yield stress and collective AC bond strength.

3. Discussion

In this study, we examined rheological factors governing cell viability in granular guest-host injectables. Spherical bare microgels behaved as HB yield stress fluids and protected cellular cargo from mechanical trauma at low shear rates. We attribute injection protection of bare microgels to the generation of plug-like flow; shear stress magnitudes measured with unidirectional rheology approached values we anticipate would damage cellular cargo at shear rates as low as 100 s^{-1} (Figure S10, Supporting Information), a factor of 10 lower than the injected shear rate of 1250 s^{-1} where we found NSC viability to be 70%. This suggests that injection protection extends well into the sub-Newtonian flow regime. Viability decreased with the increased shear rate but was not dependent on radial needle position, suggesting mechanical trauma arose from inter-microgel rearrangements (Figure 4) which must occur during the injection. For example, microgels and NSCs rearrange as they flow from large-diameter syringes or luer-lock adapters to thin needles. During rearrangement, microgels yield and NSCs experience stress magnitudes that correspond to the yield stress (Figure 5). Interestingly, the 20 Pa yield stress for 2% (w/w) microgels falls near the stress magnitudes observed to damage cells.^[35,36] For 4% (w/w) and 80 Pa yield stress microgels, we observed a decrease in viability ($p < 0.05$) relative to the 2% (w/w) microgels (Figure 7b and Figure S14c, Supporting Information), further implying that the stress magnitude cells experience during microgel yielding can damage cellular cargo.

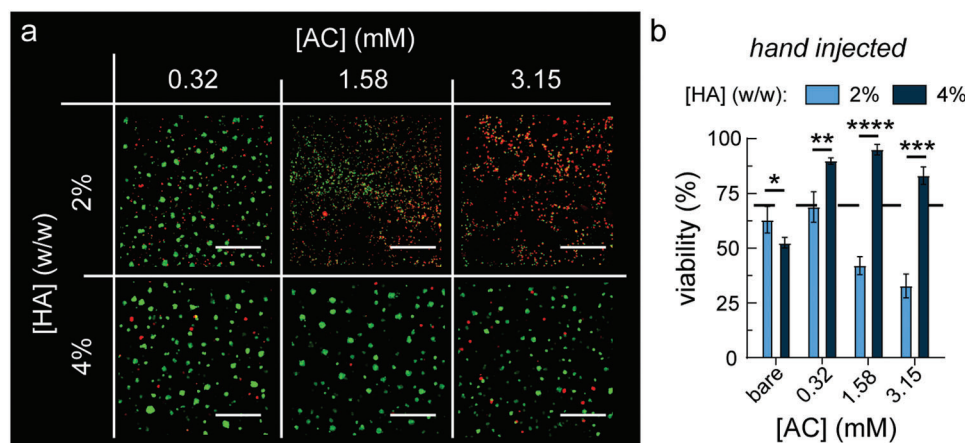


Figure 7. Injection with stiffer microgels increases NSC viability. a) Viability of NSCs after injection with 2–4% (w/w) HA microgels functionalized with 0.32–3.15 mM AC. Scale bar = 250 μm . b) Quantification of viability. Data reported as mean \pm SD ($n = 3$ samples).

These findings collectively suggest an interplay between yielding rate and microgel elasticity dictating cell viability in AC-free systems. Future studies that enable visualization of microgel architecture during high shear rate injection could provide direct support for these ideas.

We observed a small increase in viability between 2% (w/w) bare and low AC concentration microgels followed by a rapid decrease in viability for medium and high concentration AC microgels (Figure 4 and Figure S13, Supporting Information). We attribute low viability with medium and high AC concentration microgels to an inability of the microgel yield stress to support microgel dislocation associated with AC bond rupture (Figure 5). We reasoned that AC-driven microgel yielding is not supported by the bulk microgel yield stress; rupture of inter-microgel AC bonds dislocates microgels at high shear rates, damaging cellular cargo. An effective injection protecting microgel should have microgel yield stresses that exceed the stress of inter-microgel AC bond breaking, enabling new AC bonds to form and for microgels to gently roll past one another. Thus, to suppress the negative effects associated with AC-driven yielding, stiffer microgels with higher yield stresses are required. In characterizing AC bond strength, we anticipated a linear relationship between AC molecule to HA-monomer repeat unit and work of adhesion, and for additional AC bonds to behave as an increased number of elastic spring elements per unit area. However, we found that 5- and 10-fold increases in the AC molecule to HA-monomer repeat unit ratio between the low-medium and low-high AC concentrations respectively resulted in 2- and 6-fold increases in the calculated work of adhesion and 2- and 4-fold increases in adhesive stress. While this relationship should be explored further in future studies, the seemingly non-linear relationship between AC concentration and adhesion suggests that HA elasticity within the microgel could be coupled to AC bond strength. This finding indicates that internal microgel stiffness can also play a large role in granular injectable systems utilizing AC interactions and suggests that microgels can deform and store energy as AC bonds are strained. This crucial finding has implications for understanding the effect of AC bonds on other granular injectables, where cell viability has been shown to be dependent on microgel geometry.^[28] Increased engagement of AC bonds, whether through higher contact area due to changes in microgel size and geometry or AC density, leads to a non-linear elastic response whose mechanics depend heavily on yielding and intra-microgel properties.

4. Conclusion

Using a microgel platform in which we can independently control elasticity and flowability, we elucidated a mechanistic force balance between inter- and intra-microgel mechanical properties that govern stem cell viability during injection. The best-performing granular injectables had yield stresses that were greater than the stresses required to break AC bonds. Key to this discovery was our use of oscillatory rheology to probe intra-microgel mechanics and unidirectional rheology and AFM to quantify the flowability and strength of AC adhesion. Our study was also facilitated by a 3D printing-based method to screen our injection-protecting injectables, where the ability to control and observe the spatial distribution of cells during injection enabled us to explore the effect of the interplay between inter-particle

adhesion and microgel yield stress on injection protection and cell viability. We anticipate this platform to have utility in tuning injection protection and intra-tissue retention independently for an array of cell types, polymer backbones, and target tissues. This tuning capability could advance existing regenerative medicine approaches, such as cell replacement for myocardial infarction (MI) and type-1 diabetes,^[28,39–41] leveraging granular injectables.

5. Experimental Section

Cell Culture: Murine neural stem cells (NSCs) isolated from the cortices of embryonic day 15–18 C57/BL6 mice were obtained from Sigma Aldrich (SCR029). NSCs were cultured according to supplier protocols. Briefly, tissue culture dishes were coated with 20 $\mu\text{g mL}^{-1}$ poly-ornithine and 10 $\mu\text{g mL}^{-1}$ laminin stepwise overnight. Mouse NSC expansion media (Sigma Aldrich, SCM008) was used to culture NSCs on the coated tissue culture dishes and to swell the microgels. NSCs were cultured at 37 °C and 5% CO₂ in 2D where half-media changes were performed every other day until reaching 80–90% confluency. To ensure that the effects of nutrient depletion were minimized during 3D microgel culture, experiments extending beyond 24 h were supported by 50% daily media exchanges. Cells were confirmed to be negative for mycoplasma; testing occurred every 3–4 months with the Agilent MycoSensor QPCR Assay Kit.

Methacrylation of Hyaluronic Acid (HA): Methacrylated hyaluronic acid (MeHA) was prepared as described previously.^[31,32] Briefly, HA (Lifecore Biomedical, HA60K-5) with a nominal molecular weight of 60 kDa was suspended in deionized water at a maximum of 1% (w/w). The solution was continually stirred, placed on ice for the remainder of the reaction, and 8 mL of methacrylic anhydride (Sigma Aldrich, 760-93-0) per gram of HA was added dropwise (\approx 10-fold excess relative to the disaccharide repeat unit). The pH was maintained between 8–9 using NaOH for 6–8 h. The reaction is continued overnight at 4 °C to achieve 98% functionalization (Figure S1, Supporting Information). To collect the MeHA, chilled ethanol was added in 10-fold excess to the solution causing the MeHA to precipitate out. The mixture was centrifuged, ethanol was aspirated, and the MeHA was resuspended in deionized water. The resuspended MeHA was vacuum-filtered through a 0.22 μm filter to remove unreacted methacrylate anhydride. The solution was stored at -80 °C overnight and lyophilized for long-term storage. ¹H-NMR spectra were collected on a Bruker Avance AVB-400 at 400 MHz. Methacrylation efficiency was calculated as the ratio of vinylic protons on the methacrylate group to the N-acetyl methyl protons on the HA backbone, normalized to the number of protons per group (Figure S1, Supporting Information).

Microgel Fabrication and Functionalization: To fabricate HA microgels, hydrogel droplets were crosslinked in an inverse emulsion. The aqueous phase consisted of 2% (w/w) MeHA and crosslinker 1,4-dithiothreitol (DTT) with a 0.7 thiol:HA monomer repeat ratio, and the organic phase consisted of kerosene and 1.25% (w/w) Span-80 (Sigma Aldrich, S6760-250ML). The concentrations of each component in the aqueous phase were determined by fabricating bulk hydrogels and performing oscillatory rheology, where parameters that generated hydrogels with 400 Pa storage moduli were chosen to mimic the mechanical properties of the brain parenchyma (Figure S3b, Supporting Information). The resulting solution was homogenized using the Bio-Gen PRO200 (Pro Scientific, 01–01200) to create smaller and monodisperse emulsion droplets. The Michael addition reaction was performed by mixing on ice for a minimum of 4 h. Once crosslinked, the organic phase was removed from the mixture. To remove excess kerosene and surfactant, the microgels were serially washed with 0.1% (v/v) Tween 20 in PBS (Sigma Aldrich, P1379-25ML). Wash steps were performed by diluting the microgel pellet by a minimum of a factor of 1000 (v/v) for each wash.

Inter-microgel adhesion was tuned using a custom adamantane peptide (Adamantane-KKKCG) and cyclodextrin (Tocopharm, 81644-55-5). From the rheological data (Figure S3b, Supporting Information), it was

shown that centrifugation of HA microgels at 4000×g yields G' values that approach the bulk hydrogel limit. Previous studies had shown that small-strain oscillatory rheology probes intra-microgel mechanics; therefore, the MeHA concentration within each microgel was near their bulk hydrogel counterpart (2% w/w). The monodispersity and spherical geometry of the microgels (Figure S2, Supporting Information) enabled the authors to assume that they were randomly close-packed and had a solid volume fraction of 64%. Thus, the average MeHA molarity was calculated to be 28.6 mM by multiplying the intra-microgel MeHA concentration by the approximate microgel solid volume fraction and dividing by the molecular weight of MeHA (MW = 447.39 g mol⁻¹). The required molarity of adamantane (MW = 725.0 g mol⁻¹) and cyclodextrin (MW = 1151.05 g mol⁻¹) were then calculated to achieve the desired molar ratios (Table 2).

Bare microgels were centrifuged at 4000×g for 5 min, the PBS supernatant aspirated, the pack was gently pipette mixed without introducing air bubbles with a positive displacement pipette, 500 μL of the packed microgels was removed, and the microgel suspension was placed in a 1.5 mL Eppendorf tube. Adamantane stock solution is added first and left for a minimum of 2 h on a shaker. To remove unreacted molecules, the microgels were resuspended in an additional 1 mL of PBS, centrifuged at 15 000×g for 30 s, and the PBS aspirated, repeating this process six times to achieve a 1000-fold dilution of unreacted molecules. Microgels were centrifuged at 4000×g for 5 min after rinsing and the supernatant was aspirated. The functionalization was repeated and the protocol was rinsed with cyclodextrin. The microgel pellet was resuspended in 14.5 mL of NSC growth media and moved into a 15 mL centrifuge tube. The mixture was left at 4 °C overnight, centrifuged at 4000×g for 5 min, the supernatant was aspirated, and the microgels were resuspended in 14.5 mL of NSC media to achieve a 1000-fold PBS dilution before use.

Reported concentrations of 0.01 (low), 0.05 (med), and 0.11 (high) corresponded to the individual guest or host molecule to HA monomer repeat unit ratio. Thus, it was approximated that 2%, 10%, and 22% of the HA repeat units bear AC molecules. These concentrations chosen as the methacrylation protocol used here yielded 98% efficiency (Figure S1, Supporting Information) and 70% of the HA repeat units were used for DTT crosslinking. The remaining 28% of available methacrylate groups for AC provided a sufficient dynamic range of rheological properties for this HA-DTT concentration. The same procedure was used to functionalize microgels with integrin binding peptide (Anaspec, AS-62349).

Ellman's Reaction: To determine the efficiency of the protocol for AC functionalization of HA microgels, an Ellman's reaction was performed. The authors separately prepared 20 μL of microgels with 3.15 mM adamantane, 3.15 mM cyclodextrin, and 3.15 mM AC, added sequentially, as described previously. The high AC concentration microgels were chosen for this experiment to provide the most conservative approximation of the reaction efficiency due to the formulation having the lowest predicted post-functionalization methacrylate group availability. A 20 μL microgel pack was resuspended with 20 μL of fresh PBS, centrifuged the mixture at 4000×g for 5 min, and collected the supernatant. A reaction buffer (100 mM sodium phosphate, pH 8.0, 1 mM EDTA) was prepared following the manufacturer's instructions for 5,5'-dithio-bis-(2-nitrobenzoic acid) (Ellman's reagent, product no. 22 582). 200 μL of reaction buffer and 4 μL of 4 mg mL⁻¹ Ellman's reagent were added to each supernatant and the solution's absorbance was measured at 412 nm. Data were normalized to a standard curve of each solution. It was found that the unreacted adamantane and cyclodextrin in the supernatant fell below the detection threshold of 0.1 mM, thus yielding a greater than 96% reaction efficiency (Figure S8b, Supporting Information). When AC was added sequentially, 10% of the cyclodextrin added was found to be unreacted. The authors also performed this reaction on the supernatant of the sequential AC reaction after performing the rinse protocol and found that all the unreacted cyclodextrin molecules had been removed from the solution. The Ellman's reaction could not be repeated for unreacted RGD because the highest RGD concentration of 0.2 mg mL⁻¹ (0.19 mM) used in the manuscript fell near the detection threshold.

Rheology on HA Microgels and MeHA: To characterize the mechanical properties of the microgel packs, the authors performed oscillatory,

unidirectional, and step-strain rheology on an Anton Paar 302 rheometer with a 25 mm plate-plate configuration and a 1 mm gap. The microgel samples were centrifuged at 4000×g, the liquid supernatant removed, and pipette-mixed before loading onto the rheometer. Oscillatory rheology used throughout all studies applied a 1% strain across frequencies ranging between 10⁻² and 10² Hz. Unidirectional rheology was performed between shear rates of 10⁻² and 10³ s⁻¹ and the results were fit to the HB model, $\sigma = \sigma_y(1 + (\frac{\dot{\gamma}}{\dot{\gamma}_c})^p)$, where σ is the measured stress, σ_y is the yield stress, $\dot{\gamma}$ is the applied shear rate, $\dot{\gamma}_c$ is the critical shear rate at which the stress response changes from solid- to fluid-like, and p is related to flowability at high shear rates. To determine the stress relaxation capabilities of the AC microgels, a 50% step-strain was applied and the stress response was measured and the curves were fit to the power-law model, $G'_r(t) = t^{-\beta}$. Unidirectional rheology was also used to determine 15–60 mg mL⁻¹ MeHA viscosity, varying the shear rate between 10⁻² and 10² s⁻¹ (Figure S3a, Supporting Information).

AFM on HA Hydrogels: HA hydrogels were prepared by pipette mixing 2% (w/w) MeHA and 0.7 molar ratio DTT. 20 μL droplets were placed on polystyrene tissue culture dishes and immediately submerged in kerosene with 1.25% (w/w) Span80 to mimic the inverse-emulsion microgel synthesis. Samples were crosslinked for a minimum of 4 h. The organic phase was removed from the tissue culture dish and the samples were washed with PBS or PBS and 0.1% (v/v) Tween 20. The hydrogel droplet was left to swell in PBS overnight. Similarly, AC was added stepwise overnight. The AC solutions were removed before performing AFM.

Force measurements were performed on an MFP3D-BIO (Oxford Instruments) AFM using gold-coated pyrex-nitride probes (NanoWorld, PNP-Tr-AU) with nominal spring constant 0.08 N m⁻¹. Each probe was calibrated before use by the thermal method. A force trigger threshold of 1–5 nN was used, and indentation depth was limited to 2 μm. Indentation depth, d , was calculated by subtracting probe deflection from the piezoelectric motor position. All measurements were performed in PBS at room temperature. The contact and detachment points were identified for each indentation curve and were denoted by the origin and open black circle respectively (Figure 6b). The approach curve (red) was used to calculate elastic modulus, E , and the retraction curve (blue) was used to calculate adhesive work, W_a , and maximum adhesion force, F_a (Figure 6b). To calculate E , the approach curve was fit to the conical indentation variant of the Hertzian contact model given by the equation, $F = \frac{2E \tan(\alpha) d^2}{\pi(1-\nu^2)}$, where F is the force bending the cantilever, α is the probe half-angle, and ν is Poisson's ratio, which is measured separately to be 0.45 and is comparable to previous reports^[42,43] (Figure S12, Supporting Information). Using the measured Poisson ratio and manufacturer-reported probe geometry, it was found that the conical Hertzian contact model with a single fitting parameter, E , generated curves falling directly on top of the measurements (Figure 6c). During fitting, E was constrained to 0.1–5 kPa. To calculate adhesive stress, the peak adhesive force upon probe retraction, F_a , was determined. This value was divided by the maximum contact area, A_p , which was calculated based on the maximum identified probe penetration depth.

Probes were adamantane-functionalized based on published protocols.^[44] In brief, gold-thiol reactions were performed by gently submerging the gold-coated probe in 1 mM adamantane solution overnight, then thoroughly rinsing with deionized water before use. A higher adamantane density was assumed on the functionalized gold probes than on the AC functionalized hydrogels, making hydrogel-bound cyclodextrin, rather than probe-bound adamantane, the limiting factor in adhesion measurements.

3D Printing Preparations and Hand Injections: To facilitate fluorescence imaging and assaying of various shear rates within one sample preparation process, 75 μL of microgels prepared at 1×g and 75 μL of liquid media were pipetted into glass bottom 96-well plates. To ensure that the microgels settle to the bottom of the well, they were gently agitated and incubated at 37 °C for 10 min. When the NSCs reached 80–90% confluence in 2D, the cells were removed from the tissue culture dish by incubating with Accutase for 5 min. The cells in solution were placed in a 15 mL centrifuge tube and centrifuged at 200×g for 5 min. The Accutase was aspirated, and the cell pellet was diluted to achieve the desired cell density. NSCs were

gently pipette-mixed into MeHA or HA microgels that were centrifuged at $4000\times g$ for 5 min. The resulting solution of MeHA or HA microgels with NSCs was loaded into the back of a 100 μL Hamilton gas-tight syringe. The plunger was slowly pushed through the syringe until the solution reached a 30G luer-lock affixed to the syringe. Before injection through the needle, the syringe was loaded onto the 3D printer, where the pump velocity was set to the lowest experimental flow rate. The pump was jogged until a small sphere of cells and matrix formed at the needle tip. To perform hand injections, 5 μL was manually displaced in ≈ 1 s, where the shear rate was predicted to be $20\,000\text{ s}^{-1}$.

Cell Viability Measurements and Calculations: Cell viability was determined using the Live/Dead assay (Thermo Fisher, L3224) following manufacturer protocols. Live/dead images were acquired using a Zeiss LSM 710 confocal and images used in calculating feature size measurements were acquired using a Nikon TE2000-E epifluorescence microscope. Cell viability was calculated by manually isolating the central plane of the printed feature within a 3D confocal z-stack. For experiments where NSCs aggregated and single cells could not be identified to calculate viability using manufacturer protocols (Supporting Information), the authors approximated live and dead cells to occupy the same area within a given plane and performed viability calculations with the equation $\% \text{ viability} = 100\% \times \frac{\text{live cells area}}{\text{total cells area}}$. To determine the total cell area, each channel was thresholded using Otsu's method and the binary images were added together. Co-localization of the red and green channels was determined to be indicative of compromised cell membranes and excluded from the live cell population. Thus, the live cell area was calculated by subtracting the binarized dead cell channel from the live cell channel. Small fragments of cells could remain from this calculation, so areas smaller than $50\ \mu\text{m}^2$ were eliminated before calculating the live cell area. This approach was validated using the equation, $\% \text{ viability} = 100\% \times \frac{\# \text{ live cell}}{\# \text{ total cell}}$, for the microgel injectables where single cells were easily identifiable due to low cellular volume fraction and found agreement between the two methods (Figure S15, Supporting Information).

Injection into HA Hydrogels and Calculations from 3D Confocal Images: Much like the preparation of samples for AFM, 100 μL of 2% MeHA hydrogels with a 0.7 DTT molar ratio was cast onto 3 cm tissue culture dishes and submerged in kerosene to prevent evaporation and to mimic the microgel fabrication protocol used here. The samples were crosslinked for 4 h before removing the kerosene and washing with PBS and 0.1% Tween 20. The samples were allowed to swell in PBS overnight before injecting 1 μL mixtures of NSCs and HA microgel or liquid media at a flow rate of $360\ \mu\text{L h}^{-1}$, corresponding to the lowest tested shear rate of 250 s^{-1} (Figure 5a). The injections were performed by loading the mixtures into the 3D printing syringe and lowering the needle into the hydrogel at $0.1\ \text{mm s}^{-1}$ to a depth of 0.5 mm from the culture dish bottom. The needle was removed at the same low velocity to minimize damage or displacement of the injected material. Injected NSCs were cultured in this hydrogel for 24 h before introducing 4 mM calcein-AM for 4 h to visualize cells encapsulated in the retained volume, which was measured with confocal microscopy.

Imaging was performed with a $10\times$ objective with an NA of 0.45, where the sampling frequency in the X-Y plane is $1.66\ \mu\text{m}$ and $8.31\ \mu\text{m}$ in the Z-plane. Due to the difference in sampling frequency between the X-Y and Z planes, the authors interpolated and re-sampled data along the Z-axis to create cubic voxels. Morphological transformations were performed to fill the gaps between cells, and the total volume occupied by the binary image was calculated (Figure S16, Supporting Information). For data showing protrusion depth (Figure 2), the minimum and maximum z-positions were identified manually within the re-sampled 3D stack with detectable fluorescence. The minimum z-position, corresponding to the glass bottom, was designated to be $z = 0\ \mu\text{m}$, and the maximum z-position with detectable fluorescence across all RGD concentrations was determined to be $420\ \mu\text{m}$ above the glass bottom. The fluorescence data was masked on a slice-by-slice basis, where data falling at $z = 0\ \mu\text{m}$ was given a grayscale value of 1 and data falling at $z = 420\ \mu\text{m}$ was given a grayscale value of 255. Data falling on slices between the minimum and maximum z-positions was designated an intensity value between 1 and 255 based on its respective z-position. The maximum intensity projection of the 3D stack was then

taken to identify the maximum z-depth of protrusion formation as a function of RGD concentration and time.

Statistical Analysis: All statistical analyses were performed in GraphPad Prism. Unless otherwise noted, data was presented as mean \pm SD. All statistical comparisons were made using a two-tailed t-test. Significance was calculated and reported as * for $p < 0.05$, ** for $p < 0.01$, *** for $p < 0.001$, and **** for $p < 0.0001$.

Supporting Information

Supporting Information is available from the Wiley Online Library or from the author.

Acknowledgements

This work was supported by the Bayer Corporation, the National Institutes of Health (R01GM122375 to SK), and the National Science Foundation (Graduate Research Fellowships to EMC and EAD). The authors would like to thank Paul Wu, Scott Probst, Gregory Parry, and Jonathan Evans of Bayer Therapeutics and Dr. Jason Burdick, and Dr. Taimoor Qazi for stimulating conversations.

Conflict of Interest

S.K., E.M.C., and C.D.M. are co-inventors on a provisional patent application for the use of microgels in cell delivery.

Data Availability Statement

The data that support the findings of this study are available from the corresponding author upon reasonable request.

Keywords

3D bioprinting, adamantane and cyclodextrin, injectable granular hydrogels, microgels, yield stress materials

Received: May 5, 2023

Revised: August 25, 2023

Published online: September 28, 2023

- [1] H. Tan, K. G. Marra, *Materials* **2010**, *3*, 1746.
- [2] L. Zhao, M. D. Weir, H. H. K. Xu, *Biomaterials* **2010**, *31*, 6502.
- [3] M. M. Adil, T. Vazin, B. Ananthanarayanan, G. M. C. Rodrigues, A. T. Rao, R. U. Kulkarni, E. W. Miller, S. Kumar, D. V. Schaffer, *Biomaterials* **2017**, *136*, 1.
- [4] Z. Liu, H. Wang, Y. Wang, Q. Lin, A. Yao, F. Cao, D. Li, J. Zhou, C. Duan, Z. Du, Y. Wang, C. Wang, *Biomaterials* **2012**, *33*, 3093.
- [5] A. C. Gaffey, M. H. Chen, C. M. Venkataraman, A. Trubelja, C. B. Rodell, P. V. Dinh, G. Hung, J. W. Macarthur, R. V. Soopan, J. A. Burdick, P. Atluri, *J. Thorac. Cardiovasc. Surg.* **2015**, *150*, 1268.
- [6] Y. Liang, P. Walczak, J. W. M. Bulte, *Biomaterials* **2013**, *34*, 5521.
- [7] J. D. Tang, E. B. Roloson, C. D. Amelung, K. J. Lampe, *ACS Biomater. Sci. Eng.* **2019**, *5*, 2117.
- [8] B. A. Aguado, W. Mulyasasmita, J. Su, K. J. Lampe, S. C. Heilshorn, *Tissue Eng., Part A* **2012**, *18*, 806.
- [9] S. Correa, A. K. Grosskopf, H. Lopez Hernandez, D. Chan, A. C. Yu, L. M. Stapleton, E. A. Appel, *Chem. Rev.* **2021**, *121*, 11385.

- [10] C. A. Deforest, K. S. Anseth, *Nat. Chem.* **2011**, *3*, 925.
- [11] C. A. Deforest, B. D. Polizzotti, K. S. Anseth, *Nat. Mater.* **2009**, *8*, 659.
- [12] J.-A. Yang, J. Yeom, B. W. Hwang, A. S. Hoffman, S. K. Hahn, *Prog. Polym. Sci.* **2014**, *39*, 1973.
- [13] P. K. Sharma, S. Taneja, Y. Singh, *ACS Appl. Mater. Interfaces* **2018**, *10*, 30936.
- [14] P. Bertsch, M. Diba, D. J. Mooney, S. C. G. Leeuwenburgh, *Chem. Rev.* **2022**, *123*, 834.
- [15] A. Moshaverinia, C. Chen, K. Akiyama, X. Xu, W. W. L. Chee, S. R. Schrickler, S. Shi, *J. Biomed. Mater. Res., Part A* **2013**, *101*, 3285.
- [16] A. K. Grosskopf, G. A. Roth, A. A. A. Smith, E. C. Gale, H. L. Hernandez, E. A. Appel, *Bioeng. Transl. Med.* **2020**, *5*, 10147.
- [17] J. Cheng, Z. Chen, C. Liu, M. Zhong, S. Wang, Y. Sun, H. Wen, T. Shu, *Nanomedicine* **2021**, *16*, 1567.
- [18] S. He, Z. Zhang, R. Luo, Q. Jiang, Li Yang, Y. Wang, *Adv. Healthcare Mater.* **2023**, *12*, 2300029.
- [19] X. Jiang, F. Zeng, X. Yang, C. Jian, L. Zhang, A. Yu, A. Lu, *Acta Biomater.* **2022**, *141*, 102.
- [20] B. Miller, A. Hansrisuk, C. B. Highley, S. R. Caliarì, *ACS Biomater. Sci. Eng.* **2021**, *7*, 4164.
- [21] G. Chen, M. Jiang, *Chem. Soc. Rev.* **2011**, *40*, 2254.
- [22] C. D. Morley, S. T. Ellison, T. Bhattacharjee, C. S. O'bryan, Y. Zhang, K. F. Smith, C. P. Kabb, M. Sebastian, G. L. Moore, K. D. Schulze, S. Niemi, W. G. Sawyer, D. D. Tran, D. A. Mitchell, B. S. Sumerlin, C. T. Flores, T. E. Angelini, *Nat. Commun.* **2019**, *10*, 3029.
- [23] C. B. Highley, K. H. Song, A. C. Daly, J. A. Burdick, *Adv. Sci.* **2019**, *6*, 1801076.
- [24] L. Ouyang, J. P. Wojciechowski, J. Tang, Y. Guo, M. M. Stevens, *Adv. Healthcare Mater.* **2022**, *11*, 2200027.
- [25] C. D. Morley, J. Tordoff, C. S. O'bryan, R. Weiss, T. E. Angelini, *Soft Matter* **2020**, *16*, 6572.
- [26] V. G. Muir, T. H. Qazi, S. Weintraub, B. O. Torres Maldonado, P. E. Arratia, J. A. Burdick, *Small* **2022**, *18*, 2201115.
- [27] T. H. Qazi, J. Wu, V. G. Muir, S. Weintraub, S. E. Gullbrand, D. Lee, D. Issadore, J. A. Burdick, *Adv. Mater.* **2022**, *34*, 2270092.
- [28] A. E. Widener, S. Duraivel, T. E. Angelini, E. A. Phelps, *Adv. Nanobiomed Res.* **2022**, *2*, 2200030.
- [29] L. Riley, L. Schirmer, T. Segura, *Curr. Opin. Biotechnol.* **2019**, *60*, 1.
- [30] J. E. Mealy, J. J. Chung, H-Ho Jeong, D. Issadore, D. Lee, P. Atluri, J. A. Burdick, *Adv. Mater.* **2018**, *30*, 1705912.
- [31] B. Ananthanarayanan, Y. Kim, S. Kumar, *Biomaterials* **2011**, *32*, 7913.
- [32] R. A. Marklein, J. A. Burdick, *Soft Matter* **2010**, *6*, 136.
- [33] S. Grealish, E. Diguët, A. Kirkeby, B. Mattsson, A. Heuer, Y. Bramoulle, N. Van Camp, A. L. Perrier, P. Hantraye, A. Björklund, M. Parmar, *Cell Stem Cell* **2014**, *15*, 653.
- [34] S. Kriks, J.-W. Shim, J. Piao, Y. M. Ganat, D. R. Wakeman, Z. Xie, L. Carrillo-Reid, G. Auyeung, C. Antonacci, A. Buch, L. Yang, M. F. Beal, D. J. Surmeier, J. H. Kordower, V. Tabar, L. Studer, *Nature* **2011**, *480*, 547.
- [35] S. Regmi, A. Fu, K. Q. Luo, *Sci. Rep.* **2017**, *7*, 39975.
- [36] L. B. Leverett, J. D. Hellums, C. P. Alfrey, E. C. Lynch, *Biophys. J.* **1972**, *12*, 257.
- [37] B. S. Jha, M. Farnoodian, K. Bharti, *Stem Cells Transl. Med.* **2021**, *10*, 198.
- [38] T. Bhattacharjee, C. P. Kabb, C. S. O'bryan, J. M. Urueña, B. S. Sumerlin, W. G. Sawyer, T. E. Angelini, *Soft Matter* **2018**, *14*, 1559.
- [39] B. Vernon, Sung Wan Kim, You Han Bae, *J. Biomater. Sci., Polym. Ed.* **1999**, *10*, 183.
- [40] M. S. Lee, M. Lill, R. R. Makkar, *Rev. Cardiovasc. Med.* **2004**, *5*, 82.
- [41] C. Hoeg, A. Dolatshahi-Pirouz, B. Follin, *Gels* **2021**, *7*, 7.
- [42] F. Rehfeldt, A. Engler, A. Eckhardt, F. Ahmed, D. Discher, *Adv. Drug Delivery Rev.* **2007**, *59*, 1329.
- [43] A. M. Rosales, S. L. Vega, F. W. Delrio, J. A. Burdick, K. S. Anseth, *Angew. Chem., Int. Ed.* **2017**, *56*, 12132.
- [44] R. Barattin, N. Voyer, *Atomic Force Microscopy in Biomedical Research: Methods and Protocols*, (Eds: P. C. Braga, D. Ricci), Humana Press, Totowa, NJ **2011**, pp. 457–483.